Universal analytical modeling of plasmonic nanoparticles[†]

Renwen Yu,[a] Luis M. Liz-Marzán,[b,c,d] and F. Javier García de Abajo[*a,e]

Control over the optical response of metal nanoparticles and their associated plasmons is currently enabling many promising applications in areas as diverse as biosensing and photocatalysis. In this context, experiments based upon colloid synthesis and nanofabricated structures are assisted by numerical electromagnetic modeling, which supplies predictive simulations, but not the kind of physical intuition needed for exploration of new ideas, such as one finds when simple mathematical expressions can describe a problem. This *tutorial review* presents and extends a simple analytical simulation method that allows us to accurately describe the optical response of metal nanoparticles, including retardation effects, without the requirement of large computational resources. More precisely, plasmonic extinction spectra and near-field enhancement are described through a small set of real numbers for each nanoparticle shape, which we tabulate for a wide selection of common morphologies. Remarkably, these numbers are independent of size, composition, and environment. We further present a compilation of nanoplasmonic experimental data that are excellently described by the simple mathematical expressions here introduced.

Key learning points

1. Intuitive understanding of the optical response of plasmonic nanoparticles and its dependence on size, morphology, composition, and environment.
2. Mathematical separation between material optical properties (*i.e.*, dielectric functions) and other nanoparticle features (*i.e.*, size and geometry).
3. Simple mathematical expressions to describe plasmonic response at negligible computational cost, including retardation when the particle size is not small compared with light wavelength.
4. Successful explanation of existing measured nanoparticle spectra using simple analytical theory.
5. A tool for designing and optimizing applications of plasmonic nanoparticles such as biosensing.

1   Introduction

The study of metal nanoparticles has developed into a rich field of research with a plethora of applications in areas as diverse as nanomedicine (*e.g.*, drug delivery,[1] diagnosis,[2] and cancer therapy[3]) and catalysis.[4] Indeed, metal nanoparticles exhibit extraordinary optical properties inherited from the ability of their conduction electrons to sustain collective oscillations known as plasmons, which are key ingredients in those applications. Most notably, (*i*) plasmons interact strongly with light; (*ii*) they are robust against imperfections, inhomogeneities, environmental noise; (*iii*) their frequency and spatial extension are sensitive to the dielectric environment; (*iv*) the optical electric field can be largely amplified near a nanoparticle when irradiated by light tuned to one of its plasmon resonances; and (*v*) the optical enhancement can be confined down to a nanometer-sized region, much smaller than the incident light wavelength.

As an application of property (*i*), having been used for centuries to color glass (*e.g.*, the celebrated Lycurgus cup), the ability of metal nanoparticles to produce strong, selective light absorption was first recognized by Faraday's pioneering work[5]. Modern colloid synthesis and nanolithography techniques have achieved a remarkable degree of control over nanoparticle-based structural coloring.[6]

The robustness of plasmons against particle details and environmental conditions (property (*ii*)) enables the design of defect-tolerant structures for the nanoscale manipulation of optical fields. This property is partly inherited from the large number of electrons participating in the plasmon oscillation (the so-called spectral strength, which is quantified by the area under the extinction cross-section peak associated with this type of excitation), as

[a] ICFO-Institut de Ciencies Fotoniques, The Barcelona Institute of Science and Technology, 08860 Castelldefels (Barcelona), Spain. Tel: +34 653700342; Web: http://www.nanophotonics.es; E-mail: javier.garciadeabajo@nanophotonics.es
[b] Bionanoplasmonics Laboratory, CIC biomaGUNE, Paseo de Miramón 182, 20014 Donostia-San Sebastian, Spain.
[c] Ikerbasque, Basque Foundation for Science, 48013 Bilbao, Spain.
[d] CIBER de Bioingeniería, Biomateriales y Nanomedicina, CIBER-BBN, 20014 Donostia-San Sebastian, Spain.
[e] ICREA-Institució Catalana de Recerca i Estudis Avançats, Passeig Lluís Companys 23, 08010 Barcelona, Spain.

[†] Electronic Supplementary Information (ESI) available: detailed derivation of the main equations in the paper; tabulated model parameters for additional particle geometries; and additional comparisons with experiments. See DOI: 10.1039/xxx
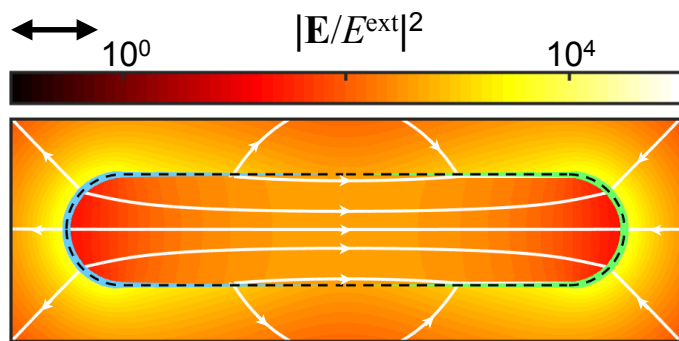
Fig. 1 Generic characteristics of nanoparticle plasmons. In an illuminated nanoparticle (contour indicated by a dashed line), under the influence of the external optical electric field $\mathbf{E}^{\text{ext}}$, conduction electrons move in an oscillatory motion back and forth between the ends of the structure, where charge piles up (blue (positive) and green (negative) curves of thickness proportional to the induced surface-charge density) and the total field $\mathbf{E}$ is enhanced (underlying density plot). The orientation of $\mathbf{E}$ (field lines, also parallel to the induced current inside the metal) is nearly perpendicular to the surface in the regions of maximum enhancement.

opposed to optical modes in smaller systems such as atoms and molecules.

The spectral sensitivity to the environment (property (*iii*)) has prompted applications in the ultrasensitive detection of biomolecules, whereby the attachment of a minuscule amount of analyte to the surface of nanoparticles functionalized with a bioreceptor produces changes in the permittivity of the environment that result in measurable redshifts in the plasmon frequencies, which in turn reveal the presence of the molecules. [1]

Plasmon field enhancement (property (*iv*)) has been exploited to amplify the interaction of molecules with light, thereby increasing the strength of optical inelastic absorption and scattering, which are signals used to detect the presence of the molecules. In particular, surface-enhanced Raman scattering (SERS) has been shown to provide chemical identification at the single-molecule level. [7–9] Additionally, plasmon-assisted molecular-absorption fingerprinting has been explored in the infrared spectral window for the detection of biomolecules. [10] These sensing techniques benefit from plasmon confinement (property (*v*)) by collecting a signal primarily due to the nanoscale region in which the analyte is attached (*i.e.*, the optical hotspot associated with a localized plasmon), while the rest of the environment (*e.g.*, the complex chemical diversity of biological fluids) produces a weaker response.

In a different context, confinement and enhancement induce strong particle-plasmon-mediated interaction between optical emitters (*e.g.*, quantum dots), which has been speculated to serve as a tool for the nanoscale implementation of quantum-optics protocols. [11] As another interesting avenue, the strong plasmonic field enhancement is extensively used to introduce nonlinearities in glasses containing dispersed metallic nanoparticles, [12] while it can also generate intrinsic frequency mixing [13] and harmonic response. [14]

1.1 Plasmon characteristics

Under the influence of the oscillatory external electric field $\mathbf{E}^{\text{ext}}$ of the incident light, conduction electrons in an illuminated nanoparticle move in its interior and give rise to charge pileup at the surface, as illustrated in Fig. 1. This charge accumulation produces in turn an enhanced electric field $\mathbf{E}$ (density plot and field lines in Fig. 1), which has maximum intensity in the proximity of the particle. The induced part of $\mathbf{E}$ is nearly perpendicular to the surface, and because of the continuity of the normal electric displacement, the magnitude of $\mathbf{E}$ is drastically reduced when moving from outside to inside the particle. Interestingly, the region where the inner field is maximum (still much smaller than the global maximum outside the metal) is roughly situated near the particle center, away from the surface charge pileup. Intuitively, this is expected because the current must be proportional to the field in the metal, which flows in such a way that the surface charge oscillates at the ends of the particle. Like $\mathbf{E}$, the induced current $\mathbf{j}^{\text{ind}}$ is divergence-less in the metal ($\nabla \cdot \mathbf{j}^{\text{ind}} = 0$), so that, in virtue of the continuity equation, there is no induced charge in the bulk of the particle. However, the current is maximum in the central region, which is also the place where there is more power dissipation ($\propto |\mathbf{E}|^2$) *via* inelastic coupling of the plasmon to electron-hole pairs in the metal. The dynamics of this type of decay is a complex process, [15] which we describe in this work through a phenomenological relaxation time τ.

Before describing rigorous electromagnetic theory, it is instructive to formulate a tutorial model that captures the main characteristics of the plasmon: we consider an effective induced charge q of mass m placed at a position $\mathbf{r}$ that oscillates as a spring of characteristic frequency ω_0. This leads to the equation of motion $md^2\mathbf{r}/dt^2 = -m\omega_0^2\mathbf{r} - (m/\tau)d\mathbf{r}/dt + (2q^2/3c^3)d^3\mathbf{r}/dt^3 + q\mathbf{E}^{\text{ext}}(t)$, where the rightmost term is the force produced by the external field $\mathbf{E}^{\text{ext}}(t) = 2\text{Re}\{\mathbf{E}^{\text{ext}}e^{-i\omega t}\}$ of frequency ω, whereas the second and third terms in the right-hand side describe inelastic damping *via* Joule losses and Abraham-Lorentz radiation, [16] respectively. Direct solution of this equation permits writing the dipole induced on the particle as $q\mathbf{r} = 2\text{Re}\{\alpha(\omega)\mathbf{E}^{\text{ext}}e^{-i\omega t}\}$, where

$$\alpha(\omega) = \frac{q^2/m}{\omega_0^2 - \omega(\omega + i\tau^{-1}) - i2q^2\omega^3/3mc^3}$$

is the particle polarizability. This conceptually simple model already incorporates a correction in the plasmon lifetime due to radiative losses in a way that is consistent with the optical theorem [17] (*i.e.*, $\text{Im}\{-1/\alpha(\omega)\} \geq 2\omega^3/3c^3$). As we show below, retardation also leads to a size-dependent shift in the plasmon frequency ω_0.

1.2 Nanoparticle synthesis

The rapid development of nanoparticles has been largely based on the remarkable advancements in the synthesis of metal nanoparticles, often using lithography but mostly based on colloid chemistry. Reliable chemical recipes have been available since the 1950's for the preparation of spherical gold and silver nanoparticles, but the 21st Century has literally seen a revolution in the ability to control particle size and shape in solution. As a re-

sult, a plethora of well-defined morphologies can be routinely obtained in large amounts, including nanorods, nanowires, bipyramids, nanocubes, nanocages, or nanoplates among others.[18] Even though the growth mechanisms are not yet completely understood, there is common agreement in the importance to separate nucleation from growth and, as a result, seeded growth methods are highly preferred, as they provide a further degree of accuracy. It should be noted that, in many of such synthesis procedures, organic additives are frequently required, and often termed shape-directing agents. These mainly include surfactants and polymers, which have been claimed to preferentially adsorb on certain crystalline facets and thereby create the required symmetry breaking for anisotropic growth.

One of the most usual examples is the seeded growth of gold nanorods,[19] in which small seeds are prepared by reduction of $HAuCl_4$ with a strong reducing agent ($NaBH_4$), in the presence of a protecting agent, typically the quaternary ammonium surfactant cetyl-trimethylammonium bromide (CTAB). The reduction of additional $HAuCl_4$ by a weak reducing agent (ascorbic acid), again in the presence of CTAB and a small amount of $AgNO_3$, leads to preferential growth in the [110] direction of the face centered cubic crystalline lattice of metallic gold. Parameters such as the nature of the surfactant, the halide counterion and the concentration of Ag^+, strongly affect the morphology of the resulting nanorods, so that the aspect ratio can be finely tuned. Interestingly, if the seeds are made in the presence of citrate, nanorods can be grown in the absence of silver, but bipyramids grow in the presence of $AgNO_3$ and HCl. On the other hand, a similar method involving iodide can lead to the growth of monodisperse triangular nanoplates.

The preparation of silver nanoparticles with different morphologies typically relies on rather different methods. Probably the most successful one has been the so-called polyol method,[20] in which the solvent (and reducing agent) is ethylene glycol or a higher order polyol, and the most common stabilizer is the polymer poly(N-vinylpyrrolidone). By adjusting reactant concentrations and temperature, cubes, plates, wires and other shapes can be readily obtained with high yield and in large amounts.

Silver has also been grown on gold nanoparticle seeds, which offers a handle to further tune size and shape, using chemistry in water, with methods closely related to those used for gold nanoparticles.[21]

1.3 Theoretical description of nanoparticle plasmons

Particle plasmons have been modeled with different levels of theory. Rigorous quantum-mechanical descriptions have been carried out from first principles, but only for small systems,[22] because these methods cannot cope with finite particles having > 100's electrons. In contrast, electromagnetic theory allows us to model the optical response for any size of the particles.[23–25]

Starting with analytical models for simple geometries,[23,24] the electromagnetic simulation of nanoparticle plasmons has progressed during the last century to produce full numerical solutions of Maxwell's equations that apply to arbitrary geometries, reaching even complex arrangements of thousands of nanoparti-

cles.[25]

Unfortunately, analytical solutions of Maxwell's equations only exist for a reduced number of geometries, such as Mie's theory[23] for spheres. In the long-wavelength limit, anisotropic nanoparticles are oftentimes described using Gans' theory for the electrostatic response of ellipsoids.[24] The collective optical behavior of particle arrays can be studied using analytical multiple-scattering theories,[26] while semi-analytical modal expansions provide a quantitative level of description for both the near and far fields.[27,28] Importantly, for any particular geometry, the plasmon resonance wavelengths and quality factors are uniquely associated with resonant values of the complex dielectric permittivity of the material.[29]

In complex geometries, numerical solution of Maxwell's equations renders full details of the response, although the required computational effort is at the limit of currently available computers when several particles are present or the structures span many light wavelengths. In this context, various numerical approaches are widely used, roughly categorized into two subsets that offer complementary advantages: volume methods (*e.g.*, finite-difference in the time domain[30] and the discrete-dipole approximation[31]), in which geometrical parametrization is easier; and boundary-element methods[32,33] (BEMs), which are computationally more efficient. A review of these methods was reported almost ten years ago for the simulation of gold nanoparticles,[34] along with a critical comparison of their relative strengths. As a useful extension of that work, we introduce here a powerful analytical model that allows us to simulate the optical response of metal nanoparticles including retardation. The advantage of this approach is twofold: it takes negligible computational effort, thus enabling the optimization of geometrical and compositional parameters through broad searches for different applications of nanoparticle plasmons; and it provides physical intuition for general problems, such as the exploration of fundamental limits to plasmon absorption, extinction, and coupling to optical emitters.

In this tutorial review, we exploit a rigorous solution of Maxwell's equations obtained by incorporating successive retardation corrections in a perturbative expansion. This allows us to calculate extinction and scattering cross-sections, as well as plasmon frequencies and lifetimes, with the help of just a few real parameters. In a related development, an analytical model was formulated for an oblate spheroid by successively including retardation corrections,[35,36] a result that we generalize in this tutorial to arbitrary morphologies. Before we discuss this method in more detail, we present an example of application in Fig. 2, where we plot the extinction cross-section of two gold bipyramids of the same morphology and aspect ratio, but with different sizes. We consider polarization parallel to the long axis of the structures, for which the spectra are characterized by a prominent long-wavelength dipole plasmon, accompanied by a weaker plasmon at shorter wavelengths; the longitudinal component of the induced current associated with the former does change sign within the metal, in contrast to the latter (see electric-field density plots). Due to the resulting sign cancellations, the shorter-wavelength feature couples less efficiently to light. Additionally, the plasmons of the larger particle are redshifted and broadened
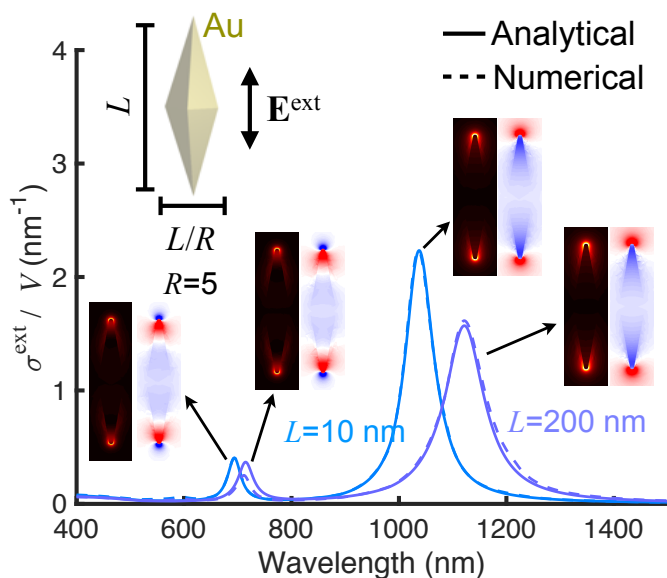
Fig. 2 Analytical description of retardation in plasmonic nanoparticles. Extinction spectra of two gold bipyramids of pentagonal cross-section, with the same aspect ratio but different size lengths L, as calculated either with our analytical model (solid curves) or from a fully numerical solution of Maxwell's equations (broken curves). Distributions of the intensity (left, thermal-color-scale plots) and instantaneous component along the long axis (right, red-blue scale for positive-negative values) of the electric field are shown for each extinction peak. The particles are assumed to be surrounded by water.

as a result of retardation, an effect that becomes less pronounced in the shorter-wavelength features, again as a result of sign cancellations in the interaction between distant induced charges, which place more weight on smaller distances. The full numerical solution of Maxwell's equations (broken curves) is nearly indistinguishable from the analytical model (solid curves), including plasmon broadening and redshifts in the larger particle. The agreement is remarkable considering that the analytical model only uses four real parameters for each particle shape and polarization direction, regardless of size (*i.e.*, four real numbers are enough to model both spectra of Fig. 2). Importantly, as we show below, retardation parameters are not obtained by fitting the numerical spectra, but rather they are calculated by integrating specific combinations of the size- and material-independent electrostatic mode fields.

2 Analytical model

2.1 Electrostatic limit

In what follows, we consider illumination with monochromatic light of frequency ω, so that the time dependence of the electric field is given by $\mathbf{E}(\mathbf{r},t) = \mathbf{E}(\mathbf{r},\omega)e^{-i\omega t} + \mathbf{E}^*(\mathbf{r},\omega)e^{i\omega t}$. Additionally, we focus on homogeneous metallic particles, with the metal described through its frequency-dependent permittivity $\varepsilon_{\mathrm{m}}(\omega)$. This is the so-called local approximation (*i.e.*, the assumption that the dielectric displacement $\varepsilon_{\mathrm{m}}(\omega)\mathbf{E}(\mathbf{r},\omega)$ depends exclusively on the electric field at the same position $\mathbf{r}$), which only breaks down for very small particles[37] (typically $< 10\,\mathrm{nm}$ for noble metals) and

also in the presence of either sharp tips or narrow gaps between metals ($< 1\,\mathrm{nm}$)[38,39].

For small particles compared with the light wavelength, retardation effects are negligible and the optical response can be simulated by solving Poisson's equation $\nabla \cdot \varepsilon(\mathbf{r},\omega)\mathbf{E}(\mathbf{r},\omega) = 0$, where $\varepsilon(\mathbf{r},\omega) = \varepsilon_{\mathrm{m}}(\omega)f(\mathbf{r}) + (1 - f(\mathbf{r}))\varepsilon_{\mathrm{h}}(\omega)$, ε_{h} is the permittivity of the host dielectric, and $f(\mathbf{r})$ is a filling function that takes a value of 1 inside the particle and 0 elsewhere. Modal expansions have been used for a long time to obtain semi-analytical formulations of this electrostatic limit.[40–44] They essentially rely on the existence of a orthogonal and complete (within the subspace of electrostatic solutions) set of real eigenmodes $\mathbf{E}_j(\mathbf{r})$ and eigenvalues ε_j labeled by j and satisfying (see Secs. I and II of the Electronic Supplemental Information, ESI)

$$\nabla \cdot \left[\varepsilon_j f(\mathbf{r}) + 1 - f(\mathbf{r}) \right] \mathbf{E}_j(\mathbf{r}) = 0.$$

In other words, $\mathbf{E}_j$ is the self-standing electrostatic field for a particle of the same geometry placed in vacuum and filled with a medium of permittivity ε_j. Eigenmodes can be normalized to satisfy the orthogonality relation (see Sec. II of the ESI)

$$\int d^3\mathbf{r}\, f(\mathbf{r})\, \mathbf{E}_j(\mathbf{r}) \cdot \mathbf{E}_{j'}(\mathbf{r}) = L^3 \delta_{jj'}, \quad (1)$$

where L is a characteristic length of the particle (*e.g.*, the diameter for a sphere or the elongation in anisotropic particles such as those of Fig. 1). Remarkably, these modes are independent of material composition. Nonetheless, they allow us to express the self-consistent electric field $\mathbf{E}(\mathbf{r},\omega)$ near an actual nanoparticle of permittivity $\varepsilon_{\mathrm{m}}(\omega)$, in response to an externally incident field $\mathbf{E}^{\mathrm{ext}}(\mathbf{r},\omega)$, as

$$\mathbf{E}(\mathbf{r},\omega) = \sum_j \left[1 - \frac{\varepsilon_{\mathrm{m}}/\varepsilon_{\mathrm{h}} - 1}{\varepsilon_j - 1} \right]^{-1} C_j^{\mathrm{ext}}(\omega)\mathbf{E}_j(\mathbf{r}), \quad (2)$$

where $\varepsilon_{\mathrm{h}}(\omega)$ is the (real, positive) permittivity of the host medium and

$$C_j^{\mathrm{ext}}(\omega) = \frac{1}{L^3} \int d^3\mathbf{r}\, f(\mathbf{r})\, \mathbf{E}_j(\mathbf{r}) \cdot \mathbf{E}^{\mathrm{ext}}(\mathbf{r},\omega).$$

The particle polarizability along a symmetry direction also admits an expansion in terms of contributions from different eigenmodes as

$$\alpha(\omega) = \frac{\varepsilon_{\mathrm{h}}}{4\pi} \sum_j V_j \left(\frac{1}{\varepsilon_{\mathrm{m}}/\varepsilon_{\mathrm{h}} - 1} - \frac{1}{\varepsilon_j - 1} \right)^{-1}, \quad (3)$$

where

$$V_j = (1/L^3) \left| \int d^3\mathbf{r}\, f(\mathbf{r})\, \mathbf{E}_j(\mathbf{r}) \right|^2 \quad (4)$$

are mode volumes, the sum of which is the total volume of the particle $\sum_j V_j = V$ in virtue of the orthonormality noted above. For example, for each of the symmery axes $l = x, y, z$ of an ellipsoid, there is only one electrostatic dipolar mode, and in turn, also only one term ($j = 1$) in eqn (3), with $V_1 = V$ and $\varepsilon_1 = 1 - 1/L_l$, where $L_l = (a_x a_y a_z / 2) \int_0^\infty ds (s + a_l^2)^{-1} [(s + a_x^2)(s + a_y^2)(s + a_z^2)]^{-1/2}$ is the corresponding depolarization factor[24] and $a_{x,y,z}$ are the half-axis
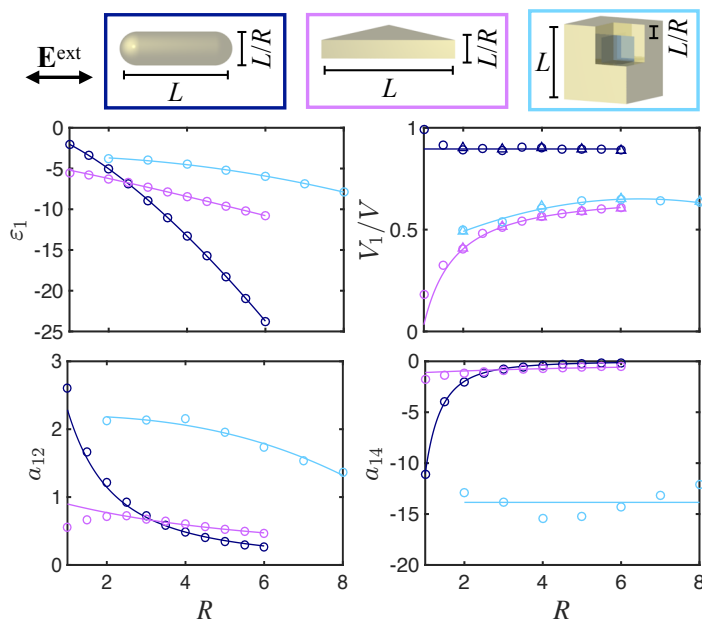
Fig. 3 Analytical model parameters for selected particle morphologies. We show the resonant permittivity ε_1, the mode volume V_1 normalized to the particle volume V, and the two retardation parameters a_{12} and a_{14} for the lowest-order dipole plasmon of rods, triangles, and cubic cages as a function of aspect ratio R. We define R and the polarization direction (double arrows) in the upper insets. Symbols for ε_1 are obtained by fitting the numerically calculated absorption spectra in the electrostatic limit. The rest of the symbols for other parameters are computed by integrating the electrostatic mode fields as shown in eqns (4) and (7), except the triangular symbols for V_1, which are extracted from the peaks in the noted spectra for comparison. Solid curves represent analytical interpolations (see Table 1). Nanorods have hemispherical caps at the tips, triangles have smooth edges with rounding radius $(1+1/R)L/40$, and cages have sharp edges and smooth corners with rounding radius $0.3L$.

lengths.

2.2 Retardation corrections

We now extend the electrostatic limit to include effects derived from the finite size of the particle relative to the free-space light wavelength λ. In particular, we use the size factor $s = \sqrt{\varepsilon_h}L/\lambda$ as a convenient perturbation parameter that already incorporates the reduction of the wavelength in the host medium relative to free space due to the refractive index $\sqrt{\varepsilon_h}$. The polarizability of eqn (3) can be corrected as (see Sec. III and IV of the ESI)

$$\alpha(\omega) = \frac{\varepsilon_h}{4\pi} \sum_j V_j B_j(s) \left(\frac{1}{\varepsilon_m/\varepsilon_h - 1} - \frac{1}{\varepsilon_j - 1} - A_j(s) \right)^{-1}, \quad (5)$$

where $A_j(s)$ and $B_j(s)$ are s-dependent functions. Here, we are interested in practice in situations for which s is not too large (see results below), so it is natural to expand these functions in power series of s. We note that the plasmon resonances are shifted and broadened due to the presence of nonzero real and imaginary parts in A_j, respectively, for which we derive the expansion (see

Sec. IV of the ESI)

$$A_j = a_{j2}s^2 + \frac{4\pi^2 i V_j}{3L^3}s^3 + a_{j4}s^4 + \dots, \quad (6)$$

where

$$a_{jn} = \frac{(2\pi i)^n}{4\pi n(n-2)! L^{n+3}} \int d^3\mathbf{r}\, f(\mathbf{r}) \int d^3\mathbf{r}'\, f(\mathbf{r}') \quad (7)$$

$$\times \left\{ (n-3)|\mathbf{r}-\mathbf{r}'|^{n-5} \left[(\mathbf{r}-\mathbf{r}') \cdot \mathbf{E}_j(\mathbf{r}) \right] \left[(\mathbf{r}-\mathbf{r}') \cdot \mathbf{E}_j(\mathbf{r}') \right] \right.$$

$$\left. + (1-n)|\mathbf{r}-\mathbf{r}'|^{n-3} \mathbf{E}_j(\mathbf{r}) \cdot \mathbf{E}_j(\mathbf{r}') \right\}.$$

Additionally, the correction in the resonance strengths (the numerator of eqn (5)) is small for the values of s under consideration (see Fig. S1 of the ESI), so we can safely approximate $B_j \approx 1$. Likewise, although retardation produces mixing of the electrostatic modes $\mathbf{E}_j$ in the electric field of eqn (2), we find that this effect is small for the values of s here considered and the main correction arises from frequency shifts and broadening captured by the expression

$$\mathbf{E}(\mathbf{r}, \omega) \approx \sum_j \left[1 - (\varepsilon_m/\varepsilon_h - 1) \left(\frac{1}{\varepsilon_j - 1} + A_j \right) \right]^{-1} C_j^{\text{ext}}(\omega) \mathbf{E}_j(\mathbf{r}). \quad (8)$$

As we show in the results presented below, we can describe the far-field scattering (through α in eqn (5)) and the near-field response (through $\mathbf{E}$ in eqn (8)) for metal nanoparticles including retardation using the electrostatic modes $\mathbf{E}_j$ together with the set of four real numbers ε_j, V_j, a_{j2} and a_{j4}.

In a recent development, an ad hoc set of quasi-normal modes has been used to account for ohmic and radiative losses for plasmonic particles.[27,45,46] These modes are obtained from solutions of the Maxwell's equations and they depend on the dielectric function of the metal. Additionally, their normalization must be taken with care, as for example in the calculation of Purcell factors.[46] In contrast, the eigenmodes of our approach are independent of the choice of metal permittivity and their normalization only involves the volume of the particle.

The resonant permittivities ε_j are found by fitting the position and strength of the peak associated with mode j in the absorption spectrum of the particle, calculated in the electrostatic limit. More precisely, we perform fully numerical calculations using BEM or a finite-element method (see below) for an airborne nanoparticle of $\sim 10\,\text{nm}$ side length (i.e., practically in the electrostatic limit), with the metal described by a simple Drude permittivity. The near field $\mathbf{E}_j$ is then taken as the induced field computed when the light frequency is tuned to the absorption maximum. Upon normalization of the field according to eqn (1), we further compute the mode volume V_j from eqn (4), and a_{j2} and a_{j4} from eqn (7). We plot these four parameters in Fig. 3 for three common morphologies (rods with hemispherical caps at the tips, equilateral triangles, and cubic cages), as a function of aspect ratio R (see upper insets). We also provide analytical R-dependent fits in Table 1. Additional sets of parameters are provided in the ESI (Fig. S2 and Table S1) for other geometries: ellipsoids, bicones,

shape	ε_1	V_1/V	a_{12}	a_{14}	V/L^3
rod	$-1.73R^{1.45}-0.296$	0.896	$6.92/(1-\varepsilon_1)$	$-11/R^{2.49}-0.0868$	$\pi(3R-1)/12R^3$
triangle	$-0.87R^{1.12}-4.33$	$-0.645R^{-1.24}+0.678$	$5.57/(1-\varepsilon_1)$	$-6.83/(1-\varepsilon_1)$	$-0.00544/R^2+0.433/R$
cage	$-0.0678R^{2.02}-3.42$	$-0.008R^2+0.103R+0.316$	$-0.00405R^{2.59}+2.21$	-13.9	$8.04/R^3-12/R^2+6/R-0.00138$

Table 1 Fitting functions for ε_1, V_1/V, a_{12}, and a_{14} corresponding to selected particle morphologies as a function of aspect ratio R (as defined in Fig. 3). The rightmost column gives the particle volume in units of L^3, including the effect of rounding in triangles and cages.
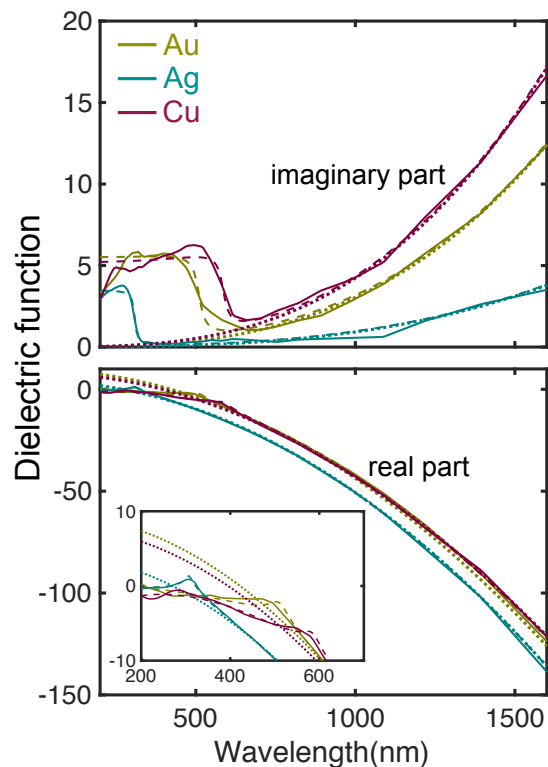

Fig. 4 Dielectric functions of noble metals. We show the dielectric functions of gold, silver, and copper taken from tabulated measured data [47] (solid curves) compared with the Drude model (eqn (9), dotted curves) and a more accurate analytical fit (dashed curves) using the parameters listed in Table 2. The inset shows a zoom of $\mathrm{Re}\{\varepsilon_m\}$ in the short wavelength region.

disks, rings, and bipyramids. The latter are used in the analytical calculations of Fig. 2. For axially symmetric structures, the electrostatic modes are obtained using the BEM, [32] whereas for other morphologies we use a finite-element method (COMSOL). As expected, we observe a trend toward larger negative values of ε_j with increasing R (i.e., with decreasing metal volume for constant length), which implies a redshift in plasmon frequency as the metal shapes are thinned. Additionally, the lowest-order plasmon mode generally contributes with a large fraction to the total volume, indicating that this is the dominant mode in the spectrum. This effect is particularly important in nanorods, and we remind again the reader that only one longitudinal dipole mode exists for electrostatic ellipsoids.

2.3 Plasmon frequency

Plasmons are associated with resonant values of the dielectric function of the metal close to one of the eigenvalues ε_j, which

are negative real numbers. Losses in actual metals are proportional to $\mathrm{Im}\{\varepsilon_m\} > 0$, implying finite plasmon lifetimes. It is instructive to approximate $\varepsilon_m(\omega) \approx \varepsilon_m(\omega_j) + \varepsilon_m'(\omega_j)(\omega - \omega_j)$ around the real frequency ω_j, defined by $\mathrm{Re}\{\varepsilon_m(\omega_j)\} = \varepsilon_h \varepsilon_j$, where the prime denotes differentiation with respect to the argument. In the absence of retardation, the complex plasmon frequency $\tilde{\omega}_j$ must satisfy $\varepsilon_m(\tilde{\omega}_j) = \varepsilon_h \varepsilon_j$, which, using the above approximation and assuming $\mathrm{Im}\{\varepsilon_m\} \ll |\varepsilon_m|$, leads to $\tilde{\omega}_j \approx \omega_j - \mathrm{i}/2\tau_j$, where $\tau_j = \mathrm{Re}\{\varepsilon_m'(\omega_j)\}/\mathrm{Im}\{\varepsilon_m(\omega_j)\}$. From the physical condition [16] $\mathrm{Re}\{\varepsilon_m + \omega\varepsilon_m'\} \geq 0$, we find $\tau_j > 0$. Additionally, the near-field intensity decays with time as $\propto |\mathrm{e}^{-\mathrm{i}\tilde{\omega}_j t}|^2 = \mathrm{e}^{-t/\tau_j}$ after the external excitation stops, clearly revealing τ_j as the plasmon lifetime.

Among common materials, the condition of relatively small $\mathrm{Im}\{\varepsilon_m\}$ is best satisfied by noble metals in the visible and near-infrared spectral regimes. In particular, gold, silver, and copper, exhibit a Drude-like response that can be characterized through the expression [48]

$$\varepsilon_m(\omega) = \varepsilon_b - \frac{\omega_p^2}{\omega(\omega + \mathrm{i}\tau^{-1})} \quad (9)$$

with parameters ε_b, ω_p, and τ as shown in Table 2. This model provides a reasonable description of the measured dielectric function [47] using constant values of ε_b for wavelengths above the interband transitions (cf. solid and dotted curves in Fig. 4). Those transitions contribute with a polarization component to the real part of ε_m (the ε_b term in eqn (9)) and also with an increase in the imaginary part (i.e., actual excitations) at short wavelengths below $\sim 370\,\mathrm{nm}$, $\sim 500\,\mathrm{nm}$, and $\sim 550\,\mathrm{nm}$ for Ag, Au, and Cu, respectively. In those regions, eqn (9) can be still applied by including an ω-dependence in ε_b, as shown in Fig. 4 (dashed curves) and Table 2 (see caption). At longer wavelengths, the lifetime of nonretarded plasmons is directly inherited from the Drude model ($\tau_j \approx \tau$).

Retardation enters through $A_j(s)$ (eqn (6)), which for small values of the size parameter s (i.e., $|A_j| \ll 1$), using eqn (9) to calculate the corresponding pole of eqn (5), leads to the complex plasmon frequency

$$\tilde{\omega}_j \approx \frac{\omega_p}{\sqrt{\varepsilon_b - \varepsilon_h \varepsilon_j}} \left[1 - \frac{A_j}{2} \frac{\varepsilon_h(\varepsilon_j - 1)^2}{\varepsilon_b - \varepsilon_h \varepsilon_j} \right] - \frac{\mathrm{i}}{2\tau}. \quad (10)$$

This expression predicts both a frequency redshift (note that the a_{j2} term in eqn (6) is positive, see Fig. 3) roughly proportional to $-\varepsilon_h(L/\lambda)^2$, accompanied by an increase in plasmon linewidth from $1/\tau$ to

$$\Delta\omega_j \approx \frac{1}{\tau} + \frac{2\pi^2 \omega_p}{3} \frac{V_j}{\lambda^3} \frac{\varepsilon_h^{5/2}(\varepsilon_j - 1)^2}{(\varepsilon_b - \varepsilon_h \varepsilon_j)^{3/2}}, \quad (11)$$

material	ε_b	$\hbar\omega_p$ (eV)	$\hbar\tau^{-1}$ (eV)	τ (fs)	A	B	C	$\hbar\omega_1$ (eV)	$\hbar\tau_1^{-1}$ (eV)	$\hbar\omega_2$ (eV)
Au	9.5	9.06	0.071	9.3	0.132	-1.755	20.43	2.43	0.0716	1.52
Ag	4.0	9.17	0.021	31	-9.71	-1.111	13.77	4.02	0.0760	18.5
Cu	8.0	8.88	0.103	6.4	-4.36	-1.655	12.31	2.12	0.0528	5.43

Table 2 Parameters entering the Drude dielectric function $\varepsilon_m(\omega) = \varepsilon_b - \omega_p^2/\omega(\omega + i\tau^{-1})$ with either a constant value of ε_b (Fig. 4, dotted curves) or with this constant replaced by an ω-dependent analytical fitting function $\varepsilon_b(\omega) = A + B \log\left[(\omega_1 - \omega - i\tau_1^{-1})/(\omega_1 + \omega + i\tau_1^{-1})\right] + C \exp(-\omega/\omega_2)$ (Fig. 4, dashed curves) for gold, silver, and copper.

where the second term accounts for the contribution of radiative damping.

3 Optical response for selected morphologies

3.1 Extinction spectra

Gold and silver nanorods are among the most common anisotropic nanoparticles, for which colloid synthesis protocols are well established.[19] Rod-like particles are also extensively fabricated by nanolithography for plasmonic studies, offering a wider versatility in the choice of material and particle location at the expense of a lower degree of control over size and defects. We thus put our analytical method to the test by comparing its ability to predict plasmons for a vast range of nanorod sizes and aspect ratios. We concentrate on modes with polarization along the length of the rods, as these are more sensitive to retardation and shape effects. Figure 5 presents a study for gold and silver nanorods (ε_m taken from measured data[47]) embedded in water ($\varepsilon_h = 1.77$). We plot extinction cross-section spectra calculated from[16]

$$\sigma^{ext}(\omega) = \frac{8\pi^2}{\sqrt{\varepsilon_h}\,\lambda} \text{Im}\{\alpha(\omega)\}, \tag{12}$$

using the polarizability of eqn (5) with the parameters of Table 1 (solid curves). These results are compared with full numerical solutions of Maxwell's equations obtained from the BEM[32] (dashed curves). We concentrate on the region around the lowest-order dipolar mode, for which the analytical model is found to be in excellent agreement with the full numerical results. In particular, it accurately predicts the redshift in plasmon energy with increasing aspect ratio R and rod length L for both metals under consideration. The redshift with R was anticipated in Fig. 3 from the evolution of the mode permittivity ε_l and is generally known to be the result of a shape-dependent depolarization. In contrast, the redshift with L originates from retardation: as the size increases, it takes longer time for the electromagnetic field generated by induced changes in one end of the rod to reach the other end, thus reducing the frequency at which they oscillate collectively. Additionally, plasmons in silver nanorods are blue shifted with respect to those in gold, for the same geometry, as a result of weaker d-band screening (i.e., ε_b is smaller in silver, see eqn (9) and Table 2). Also, gold plasmons are broader because the intrinsic lifetime τ is shorter in this material.

Transversal plasmons excited with polarization across the nanorods are typically observed in measurements of non-oriented nanoparticles. For this polarization, several modes are piled up in a narrow spectral range, so we have to include the three lowest-order ones in order to achieve good agreement similar to that of Fig. 5 with fully numerical calculations (see Fig. S4 of the ESI).

We find a similar degree of agreement between analytically and numerically calculated extinction spectra in other common types of nanoparticles, such as gold nanotriangles and cubic cages (Fig. 6), except that the additional features on the short-wavelength side of the lowest-order mode in cages are not well described with one single mode in the retardation regime, so that higher-order modes should be included for this intricate geometry. We offer additional model parameters in the ESI (Fig. S2 and Table S1) for other particle morphologies (ellipsoids, rings, bicones, disks, bipyramids, square rods, etc.), along with analytical fits as a function of the particle aspect ratio. Comparison of analytical and numerical simulations for the extinction cross-section is in excellent agreement for those geometries as well (not shown). As a whole, the analytical model and the parameters offered in this work cover most of the homogeneous metal nanoparticles investigated in the literature so far.

The spectral dependence of the low-order plasmons under consideration on the details of the geometry constitutes a relevant question that we analyze here by approximating the spectral response of anisotropic particles by the response of more symmetric ones. In particular, Fig. 7 shows excellent agreement in both line shape and absolute magnitude of the extinction for pentagonal bipyramids and bicones having the same length and metal volume. This prescription of maintaining the volume works rather well and leads to a considerable reduction in computational effort by exploiting the axial symmetry of the bicones.[32]

3.2 Plasmon wavelength and width

An overview of the resonance wavelengths for gold rods and triangles as a function of size and aspect ratio is presented in Fig. 8(A,B), where we observe again a systematic redshift with increasing L and R. A similar trend is observed for other types of particles composed of either gold (Fig. 8(C,D)) or silver (Fig. 8(E,F)). In all cases, the agreement between analytical (solid curves) and numerical (dashed curves) calculations is excellent. Remarkably, the shape and size dependence of the plasmon wavelengths are also well predicted by approximating the metal response in the Drude limit (i.e., with a constant value of ε_b to represent interband transitions (dotted curves in Fig. 8, calculated from eqn (10)).

In general, plasmons with longer lifetime emerge as narrower features in the spectra and they are associated with stronger near fields. A quantification of these properties is provided by the plasmon quality factor $Q = \omega/\Delta\omega$, which we define as the ratio of peak frequency to the FWHM of the plasmon feature in the ex-
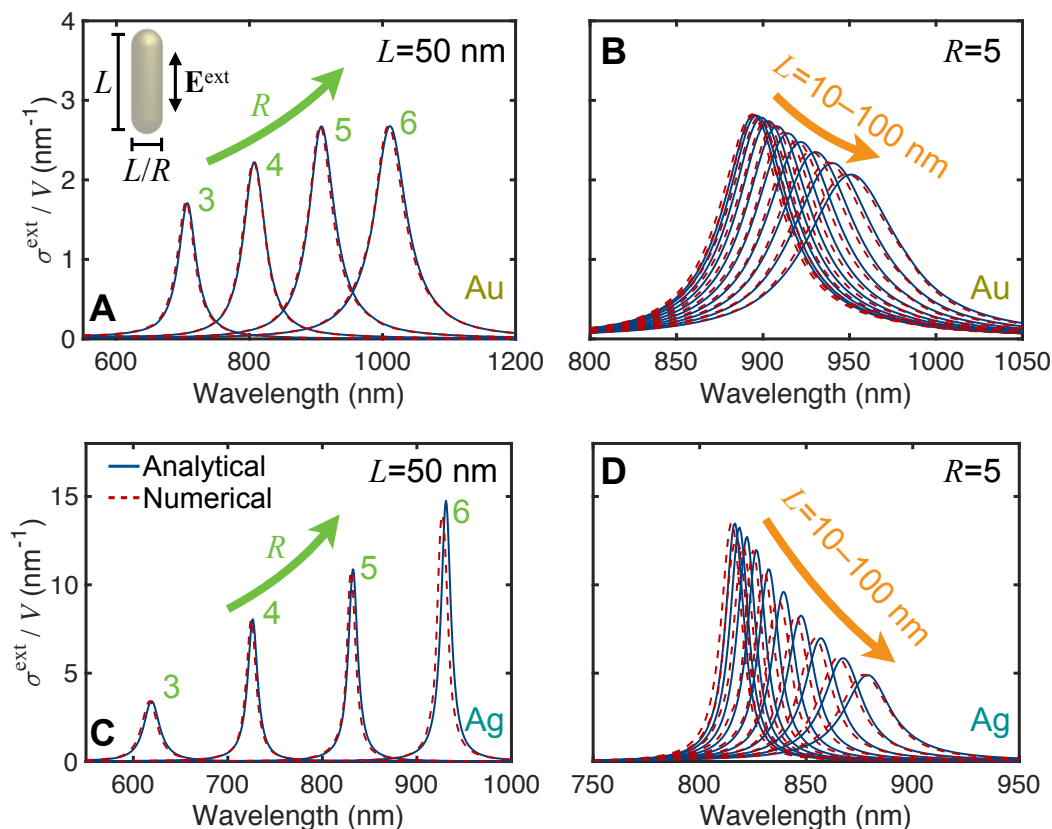
Fig. 5 Analytical description of light extinction by gold and silver nanorods. We illustrate the power of the present analytical method by comparing extinction spectra calculated either with the analytical model (solid curves) or *via* numerical solution of Maxwell's equations[32] (broken curves) for gold (A,B) and silver (C,D) nanorods immersed in water. We consider several aspect ratios R for fixed length $L = 50$ nm in (A,C) and various rod lengths L for fixed aspect ratio $R = 5$ in (B,D).
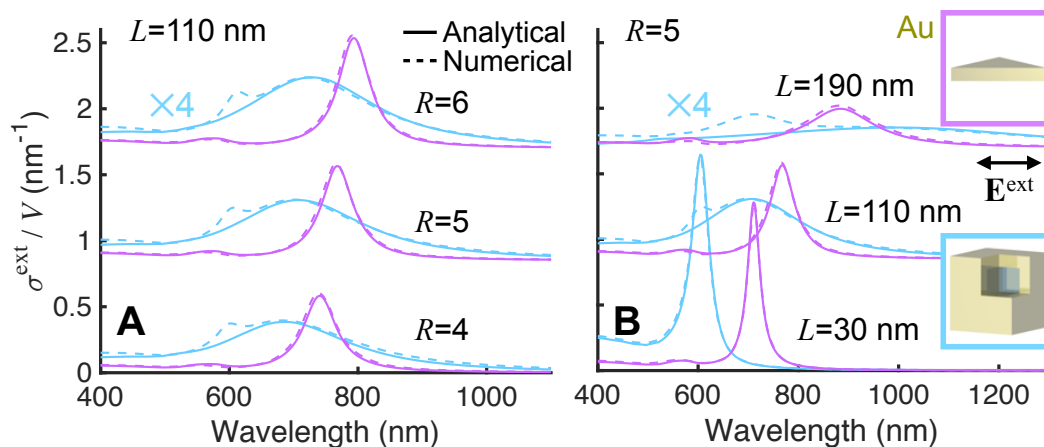

Fig. 6 Multiple plasmons revealed in the extinction spectra of gold nanotriangles and nanocages. We compare extinction spectra calculated from the analytical model (solid curves) and full numerical solutions of Maxwell's equations (dashed curves) for gold nanotriangles and nanocages immersed in water. We consider several aspect ratios R for fixed length $L = 110$ nm in (A) and various rod lengths L for fixed aspect ratio $R = 5$ in (B).
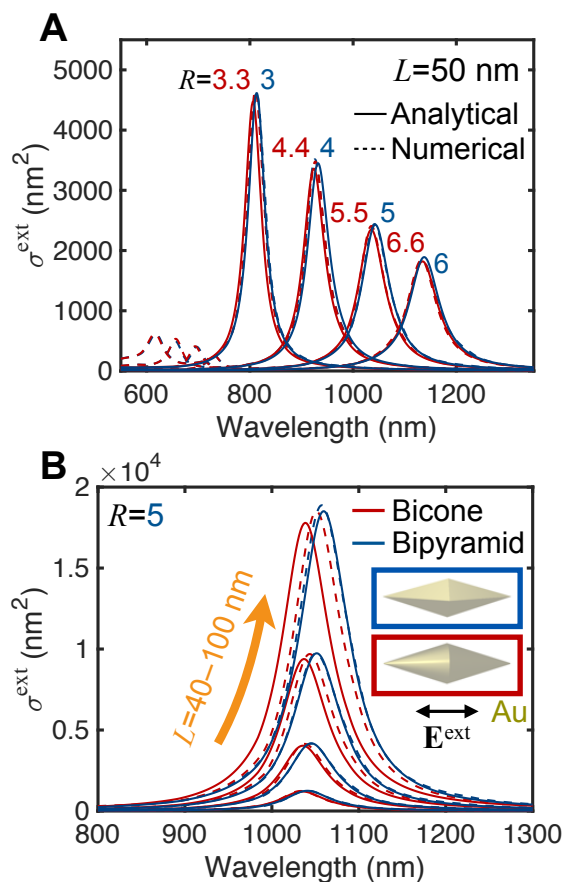
Fig. 7 Sensitivity to geometrical details. We compare the extinction cross-section of gold bicones and bipyramids of pentagonal cross-section surrounded by water. Results are shown for (A) bipyramids of fixed length $L = 50$ nm and different aspect ratios R; and (B) bipyramids of fixed aspect ratio $R = 5$ and varying length L. The corresponding bicones have the same length and metal volume, and therefore slightly different R. Full numerical electromagnetic simulations (broken curves) are compared with our analytical model (solid curves).
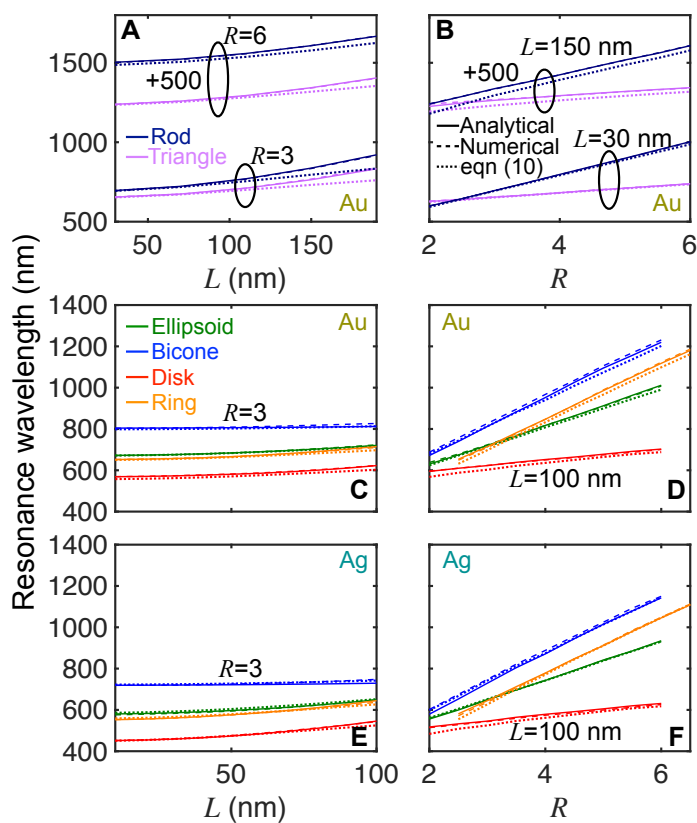

Fig. 8 Overview of the analytical model performance: plasmon wavelengths. We show the resonance wavelength corresponding to the maximum optical extinction for various types of gold nanoparticles embedded in water with either fixed aspect ratio (A,C,E) or fixed size length (B,D,F) as obtained from our analytical model (solid curves) or from fully numerical solution of Maxwell's equations (broken curves). Results from the simple Drude-model expression of eqn (10) are shown as dotted curves (plasmon wavelength taken as $2\pi c / \mathrm{Re}\{\tilde{\omega}_j\}$).
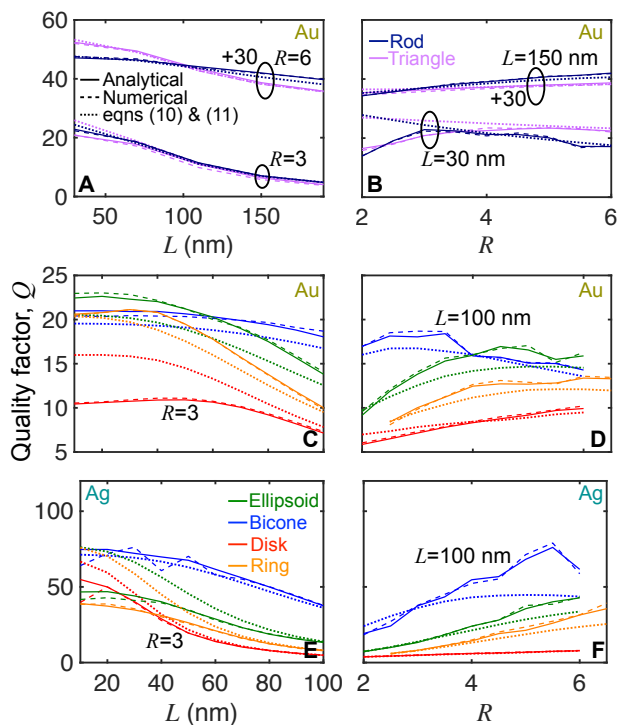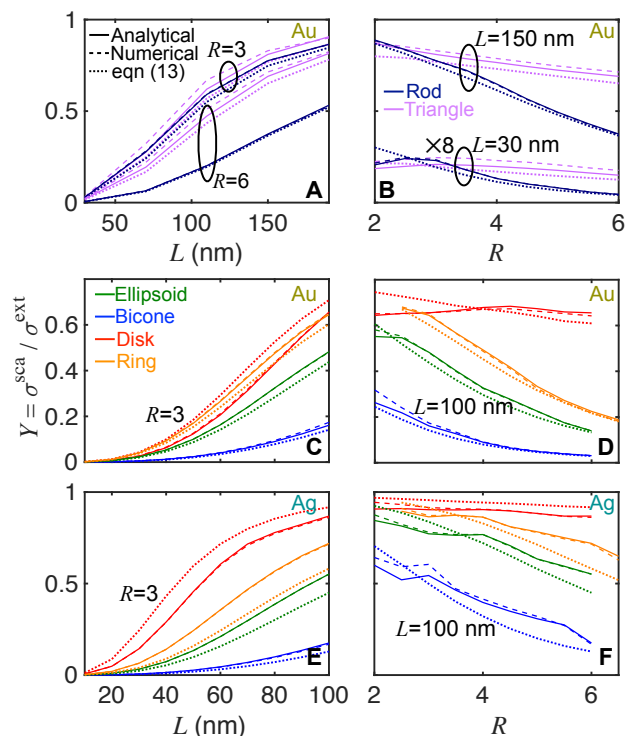
Fig. 10 Plasmon quantum yield. We show the ratio between electric-scattering and extinction cross-sections at the peak extinction frequency under the same conditions as in Fig. 8. Dotted curves correspond to the approximate expression of eqn (13), where we use the analytically fitted permittivities of Table 2 (for a frequency-dependent $\varepsilon_b(\omega)$ term).

Fig. 9 Overview of the analytical model performance: quality factors. We show the plasmon quality factor Q under the same conditions as in Fig. 8. Dotted curves are obtained from the simple analytical approximation $Q = \mathrm{Re}\{\tilde{\omega}_j\}/\Delta\omega_j$ (eqns (10) and (11)) with $\varepsilon_b = 9.5$ in (A) and (B) and with a frequency-dependent $\varepsilon_b(\omega)$ in the rest of the panels (see Table 2).

tinction spectrum. This quantity is also equal to 2π times the number of self-sustained plasmon charge oscillations before the near-field intensity decreases by a factor of e after the external illumination stops. Quality factors in the range of a few tens are common in noble metals nanoparticles, as illustrated in the summary presented in Fig. 9 for different particle morphologies and compositions. Once more, excellent agreement in plasmon width is observed between the analytical model and full numerical calculations. In contrast to the systematic redshift of the plasmon with increasing size and aspect ratio, the quality factor exhibits a more complex behavior, which can be understood from the interplay between the L and R dependences of the plasmon lifetime (see eqn (11)): for fixed R (Fig. 9(A,C,E)), the quality factor decreases with increasing L as a result of radiation losses; for fixed size (Fig. 9(B,D,F)), there is a relatively mild dependence with aspect ratio that is inherited from the redshift (higher resonant $-\mathrm{Re}\{\varepsilon_m\}$) with increasing R. Incidentally, the simple expressions of eqns (10) and (11) constitute an excellent approximation to calculate the quality factor as $Q = \mathrm{Re}\{\tilde{\omega}_j\}/\Delta\omega_j$ (Fig. 9, dotted curves), which works well for gold rods and triangles even when taking a constant value of the interband contribution to the permittivity ($\varepsilon_b = 9.5$), although a frequency-dependent $\varepsilon_b(\omega)$ (see Table 2 for a detailed expression) is necessary to obtain good agreement in the rest of the cases (Fig. 9(C-F)).

3.3 Plasmon quantum yield

Plasmons are extensively used to modify the lifetime and emission characteristics of point emitters such as molecules and quantum-dots. Before we analyze plasmon-emitter coupling in more detail (see below), let us consider an important figure of merit that characterizes plasmons in this respect: the fraction of energy emanating from them in the form of propagating light. This is the so-called quantum yield of the plasmon, which can be extracted from far-field measurements as the ratio between elastic-scattering and extinction cross-sections. For small particles described through their polarizability, the extinction cross-section is given by eqn (12), whereas the elastic scattering cross-section reduces to[17] $\sigma^{\rm sca} = (128\pi^5/3\lambda^4)|\alpha(\omega)|^2$. The ratio between these two quantities (*i.e.*, the quantum yield) then becomes

$$Y = \frac{\sigma^{\rm sca}(\omega)}{\sigma^{\rm ext}(\omega)} = \frac{16\pi^3\sqrt{\varepsilon_{\rm h}}}{3\lambda^3}\frac{1}{{\rm Im}\{-1/\alpha(\omega)\}}$$

$$\approx \left[1 + \frac{3\lambda^3}{4\pi^2\sqrt{\varepsilon_{\rm h}}V_1}{\rm Im}\left\{\frac{1}{\varepsilon_{\rm h}-\varepsilon_{\rm m}}\right\}\right]^{-1}. \qquad (13)$$

The approximate expression at the end of eqn (13) is obtained by making use of eqn (5), assuming that a single mode $j = 1$ dominates the scattering spectra. It is remarkable that the retardation parameters a_{12} and a_{14} do not appear explicitly in this result.

The quantum yield is plotted in Fig. 10 as a function of particle size and aspect ratio for gold nanorods and nanotriangles. We find again an excellent agreement between the analytical model (solid curves) and numerical electromagnetic simulations (broken curves), for which Y is computed as the ratio of cross sections at the peak frequency of $\sigma^{\rm ext}$. Additionally, excellent agreement is obtained with the analytical approximation of eqn (13) (dotted curves), using eqn (9) for $\varepsilon_{\rm m}$ with the frequency-dependent fits of $\varepsilon_{\rm b}(\omega)$ given in Table 2. These results confirm the expected increase in quantum yield with increasing particle size (Fig. 10(A)), because the radiative loss channel becomes more relevant due to stronger coupling to radiation (*i.e.*, the particle dipole roughly scales linearly with particle volume). Additionally, the quantum yield decreases with increasing aspect ratio for a fixed size (Fig. 10(B)) because of the combination of two effects: the volume is reduced, thus making the plasmon dipole smaller; and the plasmon redshift discussed above contributes to make the particle comparatively smaller in front of the emission wavelength, therefore reducing the relative contribution of radiation losses.

4 Overview comparison with experiments

We present in Fig. 11 an overview of the resonance light wavelength corresponding to gold nanoparticles of different sizes and morphologies, taken from various experimental sources (symbols) and compared with the predictions of the analytical model (curves). Despite the vast range of aspect ratios and sizes, clearly extending up to relatively large particles for which retardation effects are important, the overall agreement is rather satisfactory, thus confirming the ability of the simple analytical expressions presented above to explain and predict the measured behavior of nanoparticle plasmons.
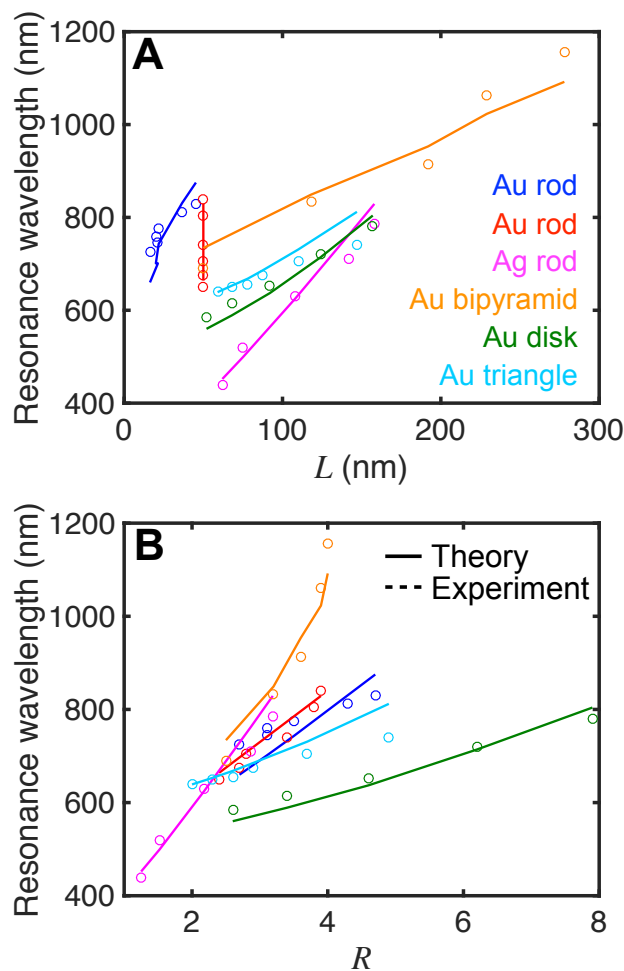

Fig. 11 Analytical model versus experiment. We plot the resonance wavelength of dipolar modes in different types of gold particles as a function of size length L (A) and aspect ratio R (B), taken from various experimental sources (symbols for rods,[49–51] bipyramids,[52] disks,[53] and triangles[54]) and compared with the predictions from the analytical model (solid curves).
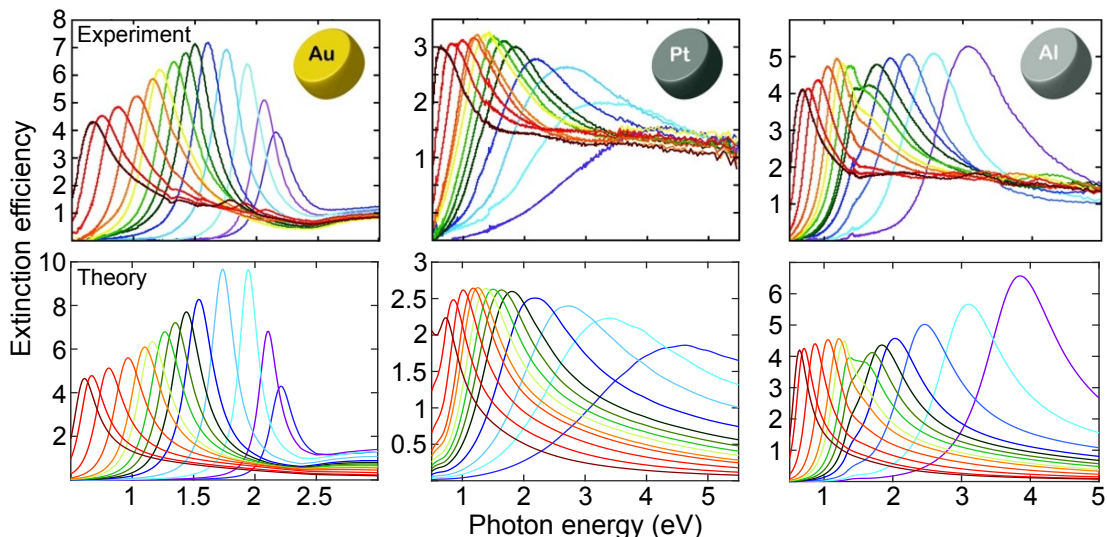
Fig. 12 Comparison of measured (upper panels) and analytically-calculated (lower panels) spectra for disks of varied sizes and compositions. We show experimental spectra taken from Zoric *et al.*[53] for disks lithographically patterned on gold, platinum, and aluminum (see insets), compared with calculations performed using our analytical model. Calculations use the measured dielectric functions for Au,[47] Pt,[55] and Al.[55] The disk thickness is 20 nm in all cases, while the disk diameter varies from ∼50-550 nm, ∼40-500 nm, and ∼70-550 nm in Au, Pt, and Al, respectively (see Fig. 2 of Ref.[53] for more details). We take the host permittivity $\varepsilon_h = 1.26$ as the average value between air and the supporting glass substrate.

We illustrate the versatility of the analytical model to cope with other types of metals in Fig. 12, where we compare experiments taken from Zoric *et al.*[53] for lithographically-patterned gold, platinum, and aluminum nanodisks (upper panels) with theory (lower panels). Excellent results are obtained, except for very small aluminum disks, where the presence of a self-limited oxide layer[53] (not accounted for in theory) can influence the optical response. We stress that the simulations are obtained using just the entries for disks in Table S1 of the ESI, which are independent of size and material, and they cover a wide range of aspect ratios $R = 2 - 27$.

Large nanoparticles of high aspect ratio present a real challenge for the analytical model because their size is not small as compared to the light wavelength. We explore this situation in Fig. 13 by comparing analytical spectra and numerical solutions of Maxwell's equations for long silver nanowires. These types of particles have been recently synthesized by growing silver on small gold nanorods, in such a way that silver is preferentially deposited along the particle tips, maintaining the wire thickness constant (∼38 nm) and reaching a total length proportional to the duration of metal reduction.[56] The agreement between theory and experiment for the plasmon-resonance wavelength is remarkable up to long wire lengths, as shown in Fig. 13(B).

In contrast to the good agreement obtained between measured and calculated plasmon light wavelengths, the plasmon widths are generally larger in experimental spectra as a result of averaging over the finite distributions of particle sizes and shapes in colloidal samples. This effect is observed in Fig. 13(B), where the calculated Q's (right scale) are found to be roughly twice the measured values. A more systematic comparison with experimental data available in the literature is offered in Fig. S3 of the ESI for the same particles considered in Fig. 11, also confirming the reduction of Q in experimental spectra. It is worth noting that

the disks of Fig. 12, fabricated using electron-beam lithography, have a smaller dispersion of size and shape,[53] and consequently, the observed and calculated widths are in closer agreement. However, the polycrystalline nature of the metal typically used in lithographic samples, which contains domain boundaries and surface defects, constitutes another source of broadening that can vary depending on the techniques used for metal growth and patterning.

5 Coupling to optical emitters

The extraordinary field enhancement and confinement produced by plasmons have been extensively used to amplify the interaction of light with molecules, quantum dots, up-conversion centers and other types of point-like optical elements. The probability associated with electronic transitions in these systems (*e.g.*, those involved in absorption by a molecule, excitation of an electronic state, and inelastic emission associated with Raman scattering) are directly proportional to the so-called local density of optical states (LDOS), which is the sum of intensities of photonic modes as a function of position and frequency.[57] Because the optical electric field is a vector, the LDOS can be defined for any direction specified through a unit vector $\hat{\mathbf{n}}$. In practice, it can be calculated from the electric field $\mathbf{E}$ generated by a unit dipole oriented along $\hat{\mathbf{n}}$ as $\text{LDOS}_{\hat{\mathbf{n}}} = \text{Im}\{\hat{\mathbf{n}} \cdot \mathbf{E}\}/(2\pi^2\omega)$, where the field is evaluated at the position of the dipole. We use this expression for the evaluation of the LDOS from full electromagnetic simulations,[32] while the analytical model leads to (see Sec. V of the ESI)

$$\frac{\text{LDOS}_{\hat{\mathbf{n}}}}{\text{LDOS}_{\hat{\mathbf{n}}}^0} \approx \frac{6\pi\sqrt{\varepsilon_h}}{k_h^3 L^3} \text{Im}\left\{ \frac{(\hat{\mathbf{n}} \cdot \mathbf{E}_1(\mathbf{r}))^2}{(1/(\varepsilon_1 - 1) + A_1)^{-1} - (\varepsilon_m/\varepsilon_h - 1)} \right\}, \quad (14)$$

where we assume a dominant mode $j = 1$.

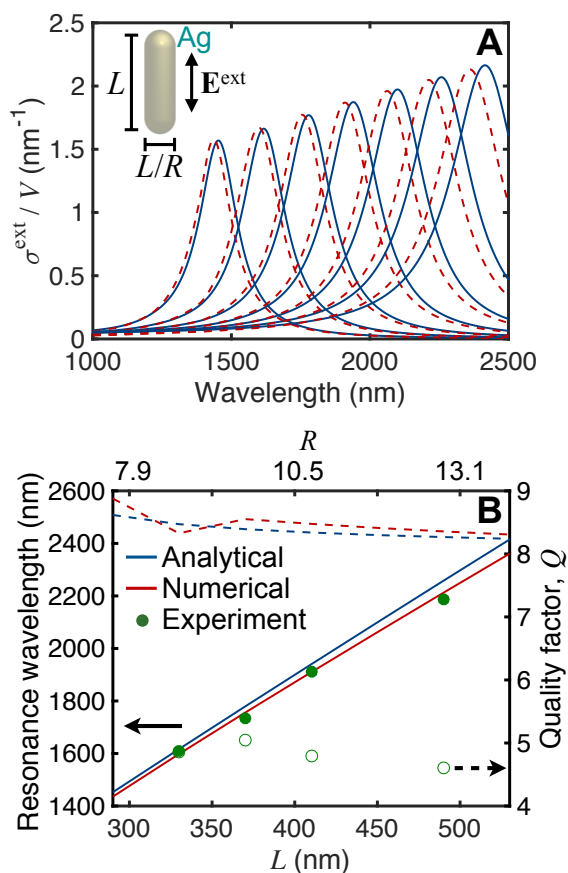We study the LDOS normalized to its value in free-space

Fig. 13 Nanorods of large aspect ratio. We show extinction spectra (A), resonant dipole-mode wavelengths (B, solid curves, left scale), and quality factors (B, dashed curves, right scale) for long silver nanorods embedded in water as calculated with the analytical model (blue curves) or *via* full solution of Maxwell's equations (red curves). The rod diameter is 38 nm in all cases. Experimental data in (B) are taken from Mayer *et al.*[56] (green symbols).
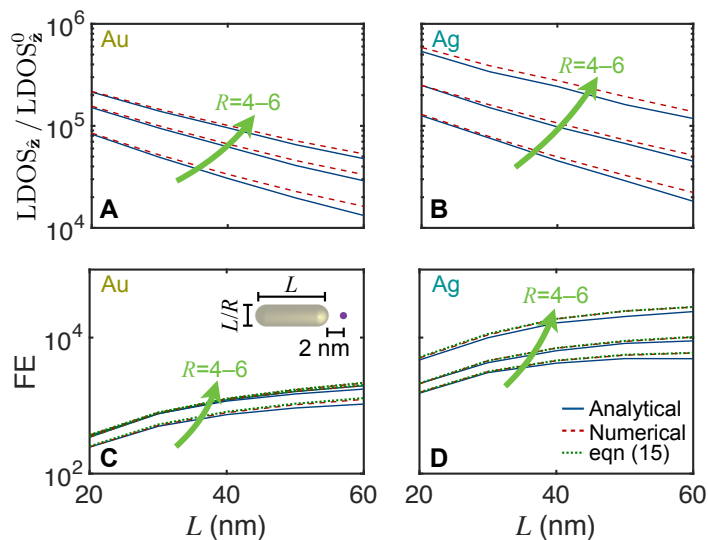

Fig. 14 Coupling between an optical emitter and a particle plasmon. (A,B) Local density of optical states (LDOS) at a frequency tuned to the lowest-order longitudinal plasmon of airborne gold (A) and silver (B) nanorods. The plotted quantity is the projection of the LDOS along the rod axis (z direction), normalized to the free-space value $\mathrm{LDOS}_{\hat{z}}^0 = \omega^2/3\pi^2 c^3$. Results are given as a function of rod length L for various aspect ratios R, with the plasmon frequency evolving with L as shown in Fig. 5. Analytical simulations (solid curves) are obtained from eqn (14) and compared with BEM numerical calculations (dashed curves). (C,D) Comparison between the field intensity enhancement (FE) calculated either from the simulated near field using the BEM (dashed curves) and from eqn (15) (solid curves, with LDOS and Y obtained from our analytical model; and dotted curves, almost identical with the dashed curves, with those quantities obtained from the BEM). LDOS and FE are referred to the position indicated by a dot in the inset of (B).

$\mathrm{LDOS}_{\hat{\mathbf{n}}}^0 = \omega^2/3\pi^2 c^3$ (this is the projection along any direction $\hat{\mathbf{n}}$, while sometimes the LDOS in vacuumm is given as the sum over all three Cartesian directions, $3\times\mathrm{LDOS}_{\hat{\mathbf{n}}}^0$) as a way to estimate the ability of plasmons to interact with optical emitters in their vicinity.

Figure 14(A,B) shows the LDOS near one of the tips of gold and silver nanorods of different aspect ratios as a function of rod length. We consider polarization $\hat{\mathbf{n}}$ along the rod long axis of symmetry and present the LDOS normalized to $\mathrm{LDOS}_{\hat{\mathbf{n}}}^0$ for a frequency corresponding to the peak of the lowest-order plasmon in their respective extinction spectra. The LDOS enhancement predicted by the analytical model is in good agreement with the result of fully numerical electromagnetic simulations, reaching values above 10^6 in silver, and roughly a factor of ~ 10 lower in gold; this is consistent with the scaling of the peak LDOS as $\propto \tau^2$ with relaxation time (see below) and the ratio $\tau_{\mathrm{Ag}}/\tau_{\mathrm{Au}} \approx 3.4$ (see Table 2), although radiative losses tend to reduce the actual ratio between total relaxation times.

As a complementary analysis, we revisit the concept of quantum yield and explore the fraction of energy transfered from an externally incident field (*e.g.*, the decay of a point emitter) to either inelastic absorption in the particle or far-field radiation emission. We thus consider the metal-absorption and radiation-emission powers P^{abs} and P^{emi}, and explore the intuitive picture that the quantum yield must be expressed as the ratio $Y = P^{\mathrm{emi}}/(P^{\mathrm{emi}} + P^{\mathrm{abs}})$. In this equation, the denominator is the total power (*i.e.*, total extinction for incident light, or decay energy for an optical point emitter), which is written as the sum of emission and absorption powers. Now, P^{abs} and P^{emi} can be analytically calculated from the current ($\propto \mathbf{E}$) induced in the metal. Using eqn (8) for $\mathbf{E}$ and assuming only one dominant plasmon mode $j = 1$, this procedure leads exactly to the same result as in eqn (13) (see Sec. VI of the ESI for more details), thus corroborating the above intuition; namely, the equivalence of obtaining the quantum yield from the ratio of scattering to extinction cross-sections or from the ratio of different power transfer channels. The latter is however more general, as it can be applied to any external source. Regarding the optical emitters considered in this section, this implies that Fig. 10 also gives the fraction of decay energy that is radiated away from the particle. And more importantly, this fraction is independent of the position of the emitter, as long as the approximation of a dominant plasmon mode is maintained; that is, the quantum yield is indeed an intrinsic property of the plasmon, independent of how it is excited, or where the emitting point element is placed.

Intuitively, one expects the field enhancement (FE, defined as the ratio of near-field to incident-field intensities) to be proportional to the increase in LDOS near the structure times the quantum yield (*i.e.*, the coupling from plasmons to radiation, which in virtue of the reciprocity principle [16] is equivalent to the coupling of radiation to plasmons). More precisely, we consider the enhancement in the component of the near field along a direction $\hat{\mathbf{n}}$ when the incident light is also polarized along that direction. This intuitive relation is demonstrated in Sec. VII of the ESI, where we conclude

$$\mathrm{FE}_{\hat{\mathbf{n}}} \approx \frac{Y}{\sqrt{\varepsilon_{\mathrm{h}}}} \frac{\mathrm{LDOS}_{\hat{\mathbf{n}}}}{\mathrm{LDOS}_{\hat{\mathbf{n}}}^0}. \tag{15}$$

This expression is tested in Fig. 14(C,D), where we find excellent agreement between the results obtained from the near field intensity calculated using the BEM (dashed curves) and the prediction of eqn (15) with the right-hand side evaluated either from the BEM (dotted curves) or from our analytical model (eqns (13) and (14)).

We stress here that the LDOS and the quantum yield Y are useful concepts of general applicability, as shown by their direct relation to the field enhancement in eqn (15). For example, the enhancement observed in SERS is roughly proportional to $(\mathrm{FE}_{\hat{\mathbf{n}}})^2 = Y^2 (\mathrm{LDOS}_{\hat{\mathbf{n}}}/\mathrm{LDOS}_{\hat{\mathbf{n}}}^0)^2$ for a Raman transition polarized along $\hat{\mathbf{n}}$, assuming a small Raman shifts (*i.e.*, the product of enhancements in both the incident light and the inelastically emitted light).

6 Summary and outlook

As a solution to the complex electromagnetic problem and the sometimes involved details of the optical response presented by metallic nanoparticles, we have reviewed and extended an analytical model capable of describing such a response accurately when compared with both state-of-the-art numerical methods and experimental data. Remarkably, each particle shape requires only four real numbers to describe the extinction spectrum, wavelength, width, and quantum yield associated with each of its plasmons. These quantities are computed by means of simple analytical expressions involving those real parameters, which are valid for any composition and size of the particles. Importantly, plasmon broadening and redshifts due to retardation are correctly described for a wide variety of particle sizes and morphologies.

The analytical model takes negligible computation time and can be readily applied to any particle shape once the noted parameters are available. As a suggested application to sensing, this method allows a fast assessment of the ability of a given nanoparticle morphology to detect changes in the dielectric environment (*i.e.*, the permittivity of the host medium ε_{h}, which enters the analytical expressions explicitly) through observed variations in the plasmonic response. Insight into inhomogeneities of a colloidal sample can be gained by comparing measurements of the optical extinction to calculated values convoluted with distributions of particle size and aspect ratio, for which the analytical model presents clear advantages. A similar optimization scheme could be applied to SERS systems. The model may also be used to engineer particle shape, in order to render a desired balance between quantum-yield and strength of coupling to localized optical emitters, with potential applications in nanoscale quantum optics. Optical heating assisted by plasmons (thermoplasmonics) may also benefit from this analytical theory. Exploration of the difference between plasmon maxima in extinction, absorption, and LDOS is also facilitated by the simplicity of the mathematical expressions.

Future extensions of this theoretical formalism should include the effect of spatial dispersion (nonlocality) and quantum confinement, which can be important when either small particles,

narrow gaps, thin films, or sharp corners and edges are considered[38,39]. A promising route to account for these effects consists in adding a nonlocal surface polarization[58], which has been successfully used for arbitrarily shaped particles[59]. Inclusion of plasmon-enhanced nonlinear optical effects also deserves an extension of the present formalism. The present theory can be readily adapted to two-dimensional materials,[43] which have recently emerged as a powerful platform for optoelectronics. Fast evaluation of the analytical model should also enable adaptive applications, for example while monitoring colloidal growth, assisted by real-time comparison with theory.

Acknowledgments

References

1   Y. L. Luo, Y. S. Shiao and Y. F. Huang, *ACS Nano*, 2011, **5**, 7796–7804.

2   J. N. Anker, W. P. Hall, O. Lyandres, N. C. Shah, J. Zhao and R. P. Van Duyne, *Nat. Mater.*, 2008, **7**, 442–453.

3   P. K. Jain, X. H. Huang, I. H. El-Sayed and M. A. El-Sayed, *Accounts Chem. Res.*, 2008, **41**, 578–1586.

4   C. Clavero, *Nat. Photon.*, 2014, **8**, 95–103.

5   M. Faraday, *Phil. Trans. R. Soc. Lond.*, 1857, **147**, 145–181.

6   R. Yu, P. Mazumder, N. F. Borrelli, A. Carrilero, D. S. Ghosh, R. A. Maniyara, D. Baker, F. J. García de Abajo and V. Pruneri, *ACS Photon.*, 2016, **3**, 1194–1201.

7   K. Kneipp, Y. Wang, H. Kneipp, L. T. Perelman, I. Itzkan, R. R. Dasari and M. S. Feld, *Phys. Rev. Lett.*, 1997, **78**, 1667–1670.

8   M. Moskovits, *J. Raman Spectrosc.*, 2005, **36**, 485–496.

9   R. A. Álvarez-Puebla, L. M. Liz-Marzán and F. J. García de Abajo, *J. Phys. Chem. Lett.*, 2010, **1**, 2428–2434.

10   O. Limaj, F. D'Apuzzo, A. Di Gaspare, V. Giliberti, F. Domenici, S. Sennato, F. Bordi, S. Lupi and M. Ortolani, *J. Phys. Chem. C*, 2013, **117**, 19119–19126.

11   R.-C. Ge and S. Hughes, *Phys. Rev. B*, 2015, **92**, 205420.

12   R. W. Boyd, *Nonlinear optics*, Academic Press, Amsterdam, 3rd edn, 2008.

13   M. Danckwerts and L. Novotny, *Phys. Rev. Lett.*, 2007, **98**, 026104.

14   O. Schwartz and D. Oron, *Nano Lett.*, 2009, **9**, 4093–4097.

15   G. V. Hartland, *Chem. Rev.*, 2011, **111**, 3858–3887.

16   J. D. Jackson, *Classical Electrodynamics*, Wiley, New York, 1999.

17   H. C. van de Hulst, *Light Scattering by Small Particles*, Dover, New York, 1981.

18   M. Grzelczak, J. Pérez-Juste, P. Mulvaney, and L. M. Liz-Marzán, *Chem. Soc. Rev.*, 2008, **37**, 1783–1791.

19   S. E. Lohse and C. J. Murphy, *Chem. Mater.*, 2013, **25**, 1250–1261.

20   M. Rycenga, C. M. Cobley, J. Zeng, W. Li, C. H. Moran,

21   Q. Zhang, D. Qin and Y. Xia, *Chem. Rev.*, 2011, **111**, 3669–3712.

21   S. Gómez-Graña, B. Goris, T. Altantzis, C. Fernández-López, E. Carbó-Argibay, A. Guerrero-Martínez, N. Almora-Barrios, N. López, I. Pastoriza-Santos, J. Pérez-Juste, S. Bals, G. Van Tendeloo and L. M. Liz-Marzán, *J. Phys. Chem. Lett.*, 2013, **4**, 2209–2216.

22   G. Onida, L. Reining and A. Rubio, *Rev. Mod. Phys.*, 2002, **74**, 601–659.

23   G. Mie, *Ann. Phys. (Leipzig)*, 1908, **25**, 377–445.

24   R. Gans, *Ann. Phys. (Leipzig)*, 1912, **37**, 881–900.

25   D. M. Solís, J. M. Taboada, F. Obelleiro, L. M. Liz-Marzán and F. J. García de Abajo, *ACS Nano*, 2014, **8**, 7559–7570.

26   F. J. García de Abajo, *Phys. Rev. B*, 1999, **60**, 6086–6102.

27   C. Sauvan, J. P. Hugonin, I. S. Maksymov and P. Lalanne, *Phys. Rev. Lett.*, 2013, **110**, 237401.

28   A. T. Anton Hörl and U. Hohenester, *ACS Photon.*, 2015, **2**, 1429–1435.

29   F. Wang and Y. R. Shen, *Phys. Rev. Lett.*, 2006, **97**, 206806.

30   A. Taflove, *Computational Electrodynamics: The Finite-Difference Time-Domain Method*, Artech House, Boston, 1981.

31   B. T. Draine and P. J. Flatau, *J. Opt. Soc. Am. A*, 1994, **11**, 1491–1499.

32   F. J. García de Abajo and A. Howie, *Phys. Rev. B*, 2002, **65**, 115418.

33   U. Hohenester and A. Trügler, *Comput. Phys. Commun.*, 2012, **183**, 370.

34   V. Myroshnychenko, J. Rodríguez-Fernández, I. Pastoriza-Santos, A. M. Funston, C. Novo, P. Mulvaney, L. M. Liz-Marzán and F. J. García de Abajo, *Chem. Soc. Rev.*, 2008, **37**, 1792–1805.

35   K. L. Kelly, E. Coronado, L. L. Zhao and G. C. Schatz, *J. Phys. Chem. B*, 2003, **107**, 668–677.

36   M. Meier and A. Wokaun, *Opt. Lett.*, 1983, **8**, 581–583.

37   U. Kreibig and M. Vollmer, *Optical Properties of Metal Clusters*, Springer-Verlag, Berlin, 1995.

38   F. J. García de Abajo, *J. Phys. Chem. C*, 2008, **112**, 17983–17987.

39   W. Zhu, R. Esteban, A. G. Borisov, J. J. Baumberg, P. Nordlander, H. J. Lezec, J. Aizpurua and K. B. Crozier, *Nat. Commun.*, 2016, **7**, 11495.

40   R. Fuchs, *Phys. Lett. A*, 1974, **48**, 353–354.

41   D. J. Bergman, *Phys. Rev. B*, 1979, **19**, 2359–2368.

42   F. Ouyang and M. Isaacson, *Philos. Mag. B*, 1989, **60**, 481–492.

43   F. J. García de Abajo, *ACS Photon.*, 2014, **1**, 135–152.

44   T. J. Davis and D. E. Gómez, *Rev. Mod. Phys.*, 2017, **89**, 011003.

45   Q. Bai, M. Perrin, C. Sauvan, J.-P. Hugonin and P. Lalanne, *Opt. Express*, 2013, **21**, 27371–27382.

46   P. T. Kristensen and S. Hughes, *ACS Photon.*, 2013, **1**, 2–10.

47   P. B. Johnson and R. W. Christy, *Phys. Rev. B*, 1972, **6**, 4370–4379.

48 N. W. Ashcroft and N. D. Mermin, *Solid State Physics*, Harcourt College Publishers, New York, 1976.

49 B. Pietrobon, M. McEachran and V. Kitaev, *ACS Nano*, 2008, **3**, 21–26.

50 L. Scarabelli, M. Grzelczak and L. M. Liz-Marzán, *Chem. Mater.*, 2013, **25**, 4232–4238.

51 H. Jia, C. Fang, X.-M. Zhu, Q. Ruan, Y.-X. J. Wang and J. Wang, *Langmuir*, 2015, **31**, 7418–7426.

52 Q. Li, X. Zhuo, S. Li, Q. Ruan, Q.-H. Xu and J. Wang, *Adv. Opt. Mater.*, 2015, **3**, 801–812.

53 I. Zoric, M. ZÃď'ch, B. Kasemo and C. Langhammer, *ACS Nano*, 2011, **5**, 2535–2546.

54 L. Scarabelli, M. Coronado-Puchau, J. J. Giner-Casares, J. Langer and L. M. Liz-Marzán, *ACS Nano*, 2014, **8**, 5833–5842.

55 E. D. Palik, *Handbook of Optical Constants of Solids*, Academic Press, San Diego, 1985.

56 M. Mayer, L. Scarabelli, K. March, T. Altantzis, M. Tebbe, M. Kociak, S. Bals, F. J. García de Abajo, A. Fery and L. M. Liz-Marzán, *Nano Lett.*, 2015, **15**, 5427–5437.

57 D. P. Fussell, R. C. McPhedran and C. Martijn de Sterke, *Phys. Rev. E*, 2004, **70**, 066608.

58 P. J. Feibelman, *Prog. Surf. Sci.*, 1982, **12**, 287–407.

59 T. Christensen, W. Yan, A.-P. Jauho, M. Soljačić and N. A. Mortensen, *Phys. Rev. Lett.*, 2017, **118**, 157402.